Digital holographic microscopy with dual-wavelength phase unwrapping

Daniel Parshall and Myung K. Kim

We apply the techniques of digital holography to obtain microscopic three-dimensional images of biological cells. The optical system is capable of microscopic holography with diffraction-limited resolution by projecting a magnified image of a microscopic hologram plane onto a CCD plane. Two-wavelength phase-imaging digital holography is applied to produce unwrapped phase images of biological cells. The method of three-wavelength phase imaging is proposed to extend the axial range and reduce the effect of phase noise. These results demonstrate the effectiveness of digital holography in high-resolution biological microscopy.   © 2006 Optical Society of America

OCIS codes: 090.1760, 100.5070, 110.0180.

1. Introduction

Digital holography is an increasingly attractive alternative to conventional holography; it replaces the photochemical processing of emulsions with digital processing of the photoelectric signals from a CCD array. It offers a number of significant advantages, such as the ability to acquire images rapidly and to apply a large number of highly effective digital processing techniques in image reconstruction. Advances in digital imaging devices such as CCD and complementary metal-oxide semiconductor cameras and in computational and data storage capacities have been central to the widening applications of digital holography. Microscopic imaging by digital holography has been applied to imaging of microstructures[1] and biological systems.[2–6] In digital holography, both the amplitude and the phase of the optical field result directly from the numerical diffraction of the optically recorded holographic interference pattern.[7–9] The numerical diffraction process can be utilized for corrections of various aberrations of the optical system such as field curvature[10] and anamorphism.[11] Digital holographic techniques have been reviewed by Schnars and Jueptner.[12]

Phase measurement is of great importance not only in holography but also in interferometry, and a large number of techniques have been developed during the long history of interferometry; more recently, digital interferometric imaging, or interferography, has been experiencing a rapid parallel progress with digital holography.[13–15] Of particular significance is the 2π-ambiguity problem in both interferometry and phase-imaging holography. A conventional approach to removing the 2π ambiguity is to apply one of many phase-unwrapping algorithms,[16,17] but often these require substantial user intervention and strict requirements on the level of phase noise and phase discontinuity. It has long been recognized that the range of unambiguous phase measurement can be extended beyond a single wavelength by synthesizing a beat wavelength between two wavelengths.[18,19] Two-wavelength phase imaging has recently been applied to digital holography.[20] Use of multiple laser wavelengths is especially advantageous in digital holography in comparison with conventional holography because of the ability to match, numerically, the exact wavelengths between recording and reconstruction. Multiwavelength digital holography has been used for full-color holography of colored objects[21,22] as well as in multicolor holographic interferometric imaging of phase objects.[23]

In this paper we present results of our experiments demonstrating the effectiveness of digital holography in biological microscopy. We have obtained microscopic images with $\sim 1 \ \mu m$ lateral resolution. Phase images of biological cells were obtained that exhibit intracellular variation of refractive indices owing to nuclei and other structures. Phase unwrapping by two-wavelength phase-imaging digital holography

The authors are with the Department of Physics, University of South Florida, Tampa, Florida 33620. M. K. Kim's e-mail address is mkkim@cas.usf.edu.
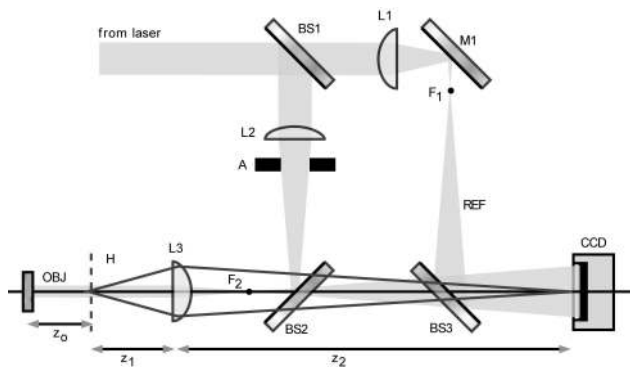
Fig. 1. Apparatus for digital holography: BS1–BS3, beam splitters and combiners; M1, mirror; OBJ, object; REF, reference; other abbreviations defined in text.

was used to remove 2π-phase discontinuities. The technique was found to be highly effective even in a biological system, in which significant phase noise would cause great difficulties for conventional phase-unwrapping techniques. In Section 2 we summarize theoretical calculations used in phase-imaging digital holography. The digital holography experiments are described in Section 3. In Section 4 we describe phase unwrapping by two-wavelength digital holography. In Section 5 multiwavelength phase imaging is extended to three wavelengths to permit a larger axial range with reduced phase noise. Consideration is also given to the possibility of complete imaging of the profiles of the front surface and the back surface as well as to refractive-index variation of a thin transparent object. Concluding remarks are given in Section 6.

2. Digital Holographic Microscopy: Theory

Here we start by using Fresnel diffraction theory to obtain expressions for optical fields at various planes in the imaging system. Refer to Fig. 1 for a schematic of the apparatus used in our experiments. A collimated beam from the laser is split into object and reference beams by beam splitter BS1. The object beam is focused by lens L2 onto point F2, which is also the front focal point of objective lens L3. Thus the object is illuminated by a collimated beam. Aperture A is placed at the conjugate point of the object with respect to L3, such that the aperture is imaged onto the object and the illumination is confined to an area of the object that is being imaged by the holographic system. This is necessary to prevent light scattered from the surrounding area of the object from entering the camera and thus contributing to the noise of the imaging system. The laser light is reflected by the object and travels toward the camera, which is placed at the point of plane H conjugate to lens L3. Hologram plane H is a distance z_0 from the object, greater than a certain minimum for the Fresnel diffraction to be valid, as discussed below. Let $E_h(x_h, y_h)$ be the two-dimensional pattern of the optical field reflected from the object at plane H. The field in front of lens L3 is[24]

$$E'(x', y') = E_h \oplus S(x', y'; z_1),\qquad(1)$$

where the point-spread function of Fresnel diffraction is

$$S(x, y; z) = -\frac{ik}{2\pi z} \exp\left[ikz + \frac{ik}{2z}(x^2 + y^2)\right],\qquad(2)$$

$\oplus$ denotes convolution, and the wavelength is $\lambda = 2\pi/k$. The field behind lens L3 of focal length f is

$$E''(x', y') = E'(x', y')\exp\left[-\frac{ik}{2f}(x'2 + y'2)\right].\qquad(3)$$

The field at the CCD plane is

$$E_c(x_c, y_c) = E'' \oplus S(x_c, y_c; z_2).\qquad(4)$$

When Eqs. (1)–(4) are combined, one obtains

$$\begin{aligned}
E_c(x_c, y_c) = &-\frac{k^2}{4\pi^2 z_1 z_2} \exp\left[ik(z_1 + z_2) + \frac{ik}{2z_2}(x_c^2\right.\\
&\left.+ y_c^2)\right]\iint dx_h dy_h E_h(x_h, y_h)\exp\left[\frac{ik}{2z_1}(x_h^2\right.\\
&\left.+ y_h^2\right]\iint dx' dy' \exp\left[\frac{ik}{2}\left(\frac{1}{z_1} + \frac{1}{z_2}\right.\right.\\
&\left.- \frac{1}{f}\right)(x'^2 + y'^2) - ik\left(\frac{x_h}{z_1} + \frac{x_c}{z_2}\right)x' - ik\left(\frac{y_h}{z_1}\right.\\
&\left.\left.+ \frac{y_c}{z_2}\right)y'\right].
\end{aligned}\qquad(5)$$

Note that the CCD is at the image plane of plane H such that

$$\frac{1}{z_1} + \frac{1}{z_2} = \frac{1}{f}, \qquad \int dx\ \exp(ikx) = 2\pi\delta(k);$$

Eq. (5) simplifies to

$$\begin{aligned}
E_c(x_c, y_c) = &-\frac{z_1}{z_2} \exp[ik(z_1 + z_2)]\exp\left[\frac{ik}{2(z_2 - f)}(x_c^2\right.\\
&\left.+ y_c^2)\right]E_h\left(-\frac{z_1}{z_2}x_h, -\frac{z_1}{z_2}y_h\right).
\end{aligned}\qquad(6)$$

The reference beam is focused by lens L1 to point F1, which is equidistant from beam combiner BS3 and point F2. This field has a spherical wavefront,

$$\exp\left[\frac{ik}{2(z_2 - f)}(x_c^2 + y_c^2)\right]$$

identical to that which would be present if a collimated beam were launched from the object side through lens L3. Therefore the field at the CCD plane

is an accurate magnified image of the field, in both amplitude and phase, that would be present if a collimated reference wave were incident upon plane H as well as on the object wave.

Suppose that the object consists of a point source located at (X_0, Y_0) on object plane (x_0, y_0) a distance z_0 from hologram plane H:

$$E_0(x_0,\ y_0) = \varepsilon_0\delta(x_0 - X_0,\ y_0 - Y_0). \qquad (7)$$

The object field at plane H is a spherical wave:

$$E_{Ho}(x_h,\ y_h) = \varepsilon_0 \exp\left\{\frac{ik}{2z_0}\left[(x_h - X_0)^2 + (y_h - Y_0)^2\right]\right\}. \qquad (8)$$

The reference field at plane H is a plane wave incident at an angle from the z axis:

$$E_{Hr}(x_h,\ y_h) = \varepsilon_r \exp[i(k_x x_h + k_y y_h)], \qquad (9)$$

where $k_x = \mathbf{k} \cdot \hat{\mathbf{x}}$ and $k_y = \mathbf{k} \cdot \hat{\mathbf{y}}$. The total field at plane H is $E_h(x_h, y_h) = E_{Ho} + E_{Hr}$, and the intensity is

$$\begin{aligned}
I_h(x_h,\ y_h) &= |E_h|^2 \\
&= |\varepsilon_r|^2 + |\varepsilon_0|^2 + \varepsilon_r\varepsilon_0{}^* \exp\left\{-\frac{ik}{2z_0}\left[(x_h - X_0)^2\right.\right. \\
&\quad \left.\left. + (y_h - Y_0)^2\right] + i(k_x x_h + k_y y_h)\right\} \\
&\quad + \varepsilon_r{}^*\varepsilon_0 \exp\left\{\frac{ik}{2z_0}\left[(x_h - X_0)^2 + (y_h - Y_0)^2\right]\right. \\
&\quad \left. - i(k_x x_h + k_y y_h)\right\}. \qquad (10)
\end{aligned}$$

In digital holography, the intensity pattern is sampled at $(x_h, y_h) = \{(\alpha\Delta, \beta\Delta); \alpha, \beta = 0, 1, 2, \cdots, N_x - 1\}$ by the CCD array of $N_x \times N_x$ and effective size $a_x \times a_x$, with $a_x = N_x\Delta$:

$$\begin{aligned}
I_h(\alpha,\ \beta) &= |\varepsilon_r|^2 + |\varepsilon_0|^2 + \varepsilon_r\varepsilon_0{}^* \exp\left\{-\frac{ik}{2z_0}\left[(\alpha\Delta - X_0)^2\right.\right. \\
&\quad \left.\left. + (\beta\Delta - Y_0)^2\right] + i(\alpha k_x + \beta k_y)\Delta\right\} \\
&\quad + \varepsilon_r{}^*\varepsilon_0 \exp\left\{\frac{ik}{2z_0}\left[(\alpha\Delta - X_0)^2 + (\beta\Delta - Y_0)^2\right]\right. \\
&\quad \left. - i(\alpha k_x + \beta k_y)\Delta\right\}. \qquad (11)
\end{aligned}$$

The first two terms in Eq. (11) are the zero-order terms that are due to the reference and object beams, which can be eliminated by a few different methods. The phase-shifting digital holography removes the zero-order and twin images through multiexposure holographic recording while the phase of reference field is shifted by an integer fraction of 2π.[25,26] An off-axis hologram spatially separates the holographic images away from the undiffracted zero order. We use the off-axis geometry and also take separate exposures of reference and object waves and subtract these from the original holographic exposure. This method proves to be highly effective in reducing any noise from these terms, although the off-axis configuration reduces the available spatial-frequency bandwidth by half. The other two terms are the holographic twin images, and these can be separated if the off-axis angle of the reference beam is large enough. We take the third term as the holographic image term. Numerical reconstruction of the holographic image starts with multiplication by a conjugate reference field:

$$\begin{aligned}
H(\alpha,\ \beta) &\equiv I_h(\alpha,\ \beta)E_{Hr}{}^*(\alpha,\ \beta) \\
&= |\varepsilon_r|^2\varepsilon_0{}^* \exp\left\{-\frac{ik}{2z_0}\left[(\alpha\Delta - X_0)^2 + (\beta\Delta\right.\right. \\
&\quad \left.\left. - Y_0)^2\right]\right\}. \qquad (12)
\end{aligned}$$

Numerical diffraction is calculated by convolution of H with S over a distance z_i to obtain the holographic image over a grid of the same size and resolution as the CCD array $(x_i, y_i) = \{(\gamma\Delta, \delta\Delta); \gamma, \delta = 0, 1, 2, \cdots, N_x - 1\}$:

$$\begin{aligned}
E_i(\gamma,\ \delta) &= H \oplus S(\gamma,\ \delta; z_i) \\
&= -\frac{ik}{2\pi z_i} \exp(ikz_i) \sum_{\alpha, \beta=0}^{N_x-1} \Delta^2 H(\alpha,\ \beta) \\
&\quad \times \exp\left\{\frac{ik\Delta^2}{2z_i}\left[(\alpha - \gamma)^2 + (\beta - \delta)^2\right]\right\}. \quad (13)
\end{aligned}$$

The image at $z_i = z_0$ is

$$\begin{aligned}
E_i(\gamma,\ \delta) &= -\frac{ik\Delta^2}{2\pi z_i} |\varepsilon_r|^2\varepsilon_0{}^* \exp(ikz_i) \\
&\quad \times \exp\left\{\frac{ik}{2z_0}\left[(\gamma^2\Delta^2 - X_0{}^2) + (\delta^2\Delta^2 - Y_0{}^2)\right]\right\} \\
&\quad \times \sum_{\alpha, \beta=0}^{N_x-1} \exp\left\{-\frac{ik\Delta}{z_0}\left[\alpha(\gamma\Delta - X_0)\right.\right. \\
&\quad \left.\left. + \beta(\delta\Delta - Y_0)\right]\right\} \\
&= -\frac{ik\Delta^2}{2\pi z_i} |\varepsilon_r|^2\varepsilon_0{}^* \exp(ikz_i) \\
&\quad \times \exp\left\{\frac{ik}{2z_0}\left[(\gamma^2\Delta^2 - X_0{}^2) + (\delta^2\Delta^2 - Y_0{}^2)\right]\right\} \\
&\quad \times \exp\left\{-\frac{ika_x}{2z_0}\left[(\gamma\Delta - X_0) + (\delta\Delta - Y_0)\right]\right\} \\
&\quad \times \frac{\sin(ka_x/2z_0)(\gamma\Delta - X_0)}{\sin(k\Delta/2z_0)(\gamma\Delta - X_0)} \\
&\quad \times \frac{\sin(ka_x/2z_0)(\delta\Delta - Y_0)}{\sin(k\Delta/2z_0)(\delta\Delta - Y_0)}
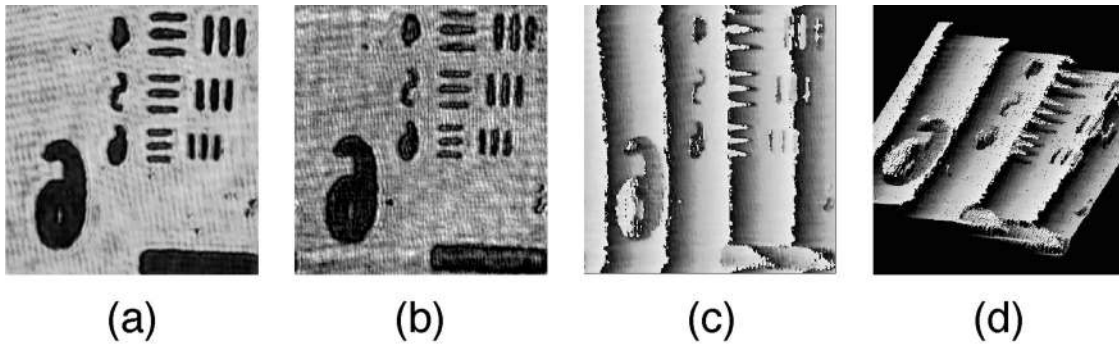\end{aligned}$$

Fig. 2. High-resolution holographic image reconstruction of the resolution target of area 88 μm × 88 μm with 360 × 360 pixels: (a) direct image when the object is on plane H, illuminated by a laser; (b) reconstructed amplitude image; (c) phase image; (d) phase image in perspective view.

$$\approx -\frac{ika_x^2}{2\pi z_i} \, |\varepsilon_r|^2 \varepsilon_0^* \exp(ikz_i)\delta_{\gamma, X_0/\Delta}\delta_{\delta, Y_0/\Delta}. \quad (14)$$

The Kronecker delta in the last line follows from the $\sin N\theta / \sin \theta$ factors, which are familiar from the theory of diffraction by a grating. The width of the Kronecker delta is $d_\gamma = 2\lambda z_0 / N_x \Delta^2$ pixels, i.e., d_γ pixels for $(ka_x/2z_0)(\gamma\Delta - X_0)$ to span $-\pi$ to $+\pi$. The discrete summation is in fact periodic and can lead to aliasing unless $(k\Delta/2z_0)(\gamma\Delta - X_0) < \pi$ for all γ, which is satisfied if

$$z_0 > \frac{a_x^2}{N_x\lambda}. \quad (15)$$

This sets the minimum object-to-hologram distance for Fresnel diffraction to be valid. We may also note at this point that the use of the convolution method maintains the pixel size of the reconstructed image identical to that of the CCD plane. If instead the Fresnel transform method is used, the pixel size varies in proportion to the distance and wavelengths. Although the amplitude image can be interpolated to maintain constant image and pixel size, interpolation of the phase image can be problematic. Methods have been developed for handling this problem by zero padding[27] or by introduction of an intermediate plane.[28]

3. Digital Holographic Microscopy: Experiment

The digital holography experiment proceeds as follows, described by use of an exemplary set of parameters: The wavelength is $\lambda = 0.532$ μm. An area of the object is chosen for imaging with $a_x = 88$ μm and $N_x = 360$, so $\Delta = 0.24$ μm. This gives $\min(z_0) = 40$ μm, and z_0 is set to this value. This area of plane H is imaged by a microscope objective onto the CCD with lateral magnification $M = 37$, to correspond to the physical pixel size of $M\Delta = 9$ μm and $Ma_x = 3.3$ mm. The resolution of the imaging system given by the Rayleigh criterion is $d = 1.22\lambda/2$ N.A. $= 0.82$ μm with an $f = 8.55$ mm microscope objective lens with a N.A. of 0.4. This corresponds to $Md = 30$ μm at the CCD. The width of the point-spread function of the digital reconstruction is $d_\gamma\Delta = 0.48$ μm, which again is smaller than the optical point-spread function d, and therefore the resolutions of the CCD array and the numerical reconstruction are all sufficient for the given optical system. The optical system described here provides a straightforward means for high-resolution holographic microscopic imaging. There is no need for elaborate processing such as magnification by using a reconstruction wavelength that is long compared with the recording wavelength,[12] which inevitably introduces aberration, or using an aperture array in front of the camera and scanning it to artificially increase the CCD resolution.[29]
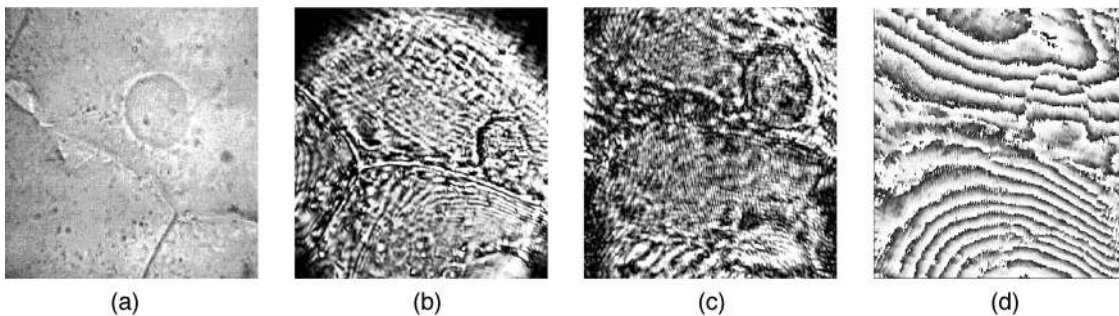
Figures 2 and 3 illustrate some of the images ob-

Fig. 3. Holographic imaging of onion cells of area 88 μm × 88 μm with 360 × 360 pixels: (a) conventional microscope image, whose scale is somewhat different from those of the holographic images; (b) direct image; (c) amplitude image; (d) phase image.
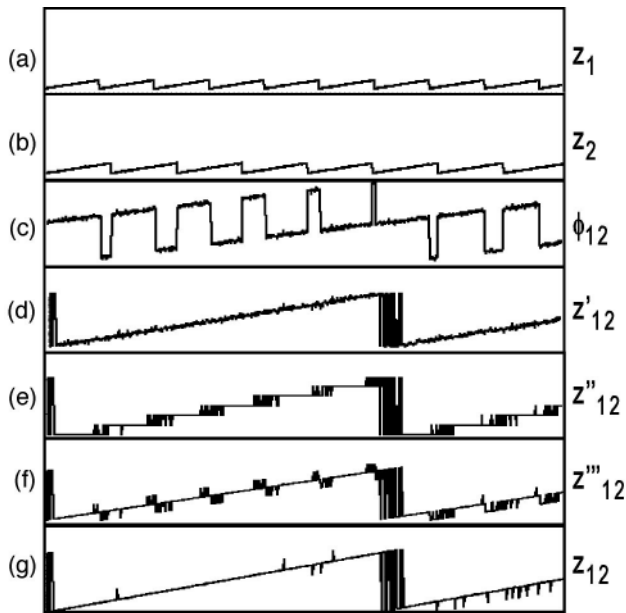
Fig. 4. Simulation of two-wavelength phase-imaging digital holography: (a) height profile $z_1(x)$ of a 10 μm high incline, derived from phase $\varphi_1(x)$ of $\lambda_1 = 0.532$ μm; (b) $z_2(x)$ derived from phase $\varphi_2(x)$ of $\lambda_2 = 0.633$ μm; (c) difference phase map $\varphi_{12}' = \varphi_1 - \varphi_2$; (d) coarse map, $z_{12}'(x)$, with beat wavelength $\Lambda_{12} = 3.33$ μm; (e) $z_{12}''(x)$, where $z_{12}'(x)$ is divided into integer multiples of λ_1; (f) $z_{12}'''(x)$, where $z_1(x)$ is pasted onto $z_{12}''(x)$; (g) fine map, $z_{12}(x)$, where most of the spikes in $z_{12}''(x)$ are removed by comparison with $z_{12}'(x)$. The vertical axis is 5.0 μm full scale in every figure, except for (c), where the vertical range is -2π to $+2\pi$.

tained from our digital holography system. Figure 2 shows an 88 μm × 88 μm area of a U.S. Air Force resolution target. Element 6 of group 7 has a 2.2 μm bar width, and the resolution of the image appears somewhat better than that, say 1 μm. The holographic amplitude image, Fig. 2(b), is quite indistinguishable from the direct image, Fig. 2(a). Also note that the phase image, Fig. 2(c) or 2(d), appears less noisy than the amplitude image. The amplitude image reflects the intensity variations in the reference wave, whereas the phase noise comes mostly from the quality of the optical surfaces in the imaging system. The former is much more difficult to control. Also note that, from the phase image, the thickness of the chrome coating on the glass plate of the resolution target is easily measured to be ~75 nm. Figure 3 shows an 88 μm × 88 μm area of a layer of onion cells. Again the amplitude images quite closely resemble the direct images. The phase images, especially Fig. 3(d), have much less noise than the amplitude image, and one can readily discern the index variation over the nucleus of the onion cell.

4. Two-Wavelength Phase-Imaging Digital Holography

The basic principle of multiwavelength phase imaging is described by reference to Fig. 4, with numerical values that were used in generating the simulation plots. Suppose that the object is a tilted plane of height $h = 5.0$ μm. A single-wavelength phase image

has 2π discontinuity wherever the height is a multiple of the wavelength. For wavelength $\lambda_1 = 0.532$ μm or $\lambda_2 = 0.633$ μm, phase map $\varphi_m(x)$ $(m = 1, 2)$ converted to surface profile $z_m(x) = \lambda_m\varphi_m/2\pi$ will consist of a number of ramps of height equal to the wavelength, Figs. 4(a) and 4(b). Subtraction of the two phase maps $\varphi_{12}' = \varphi_1 - \varphi_2$ has numerous discontinuities of 2π, Fig. 4(c), but adding 2π wherever $\varphi_{12}' < 0$ yields a new phase map, $\varphi_{12}(x) = \varphi_{12}' + 2\pi(\varphi_{12}' < 0)$, with a longer range free of discontinuities. In fact the new phase map is equivalent to that of a longer beat wavelength, $\Lambda_{12} = \lambda_1\lambda_2/|\lambda_1 - \lambda_2| = 3.33$ μm, and the corresponding surface profile is the coarse map, $z_{12}'(x) = \Lambda_{12}\varphi_{12}(x)/2\pi$, Fig. 4(d). By proper choice of the two wavelengths, axial range Λ_{12} can be adjusted to any value that would fit the axial size of the object being imaged.

This technique provides a straightforward and efficient phase-imaging method in a wide range of applications. A limitation is that any phase noise in each single-wavelength phase map is amplified by a factor equal to the magnification of the wavelengths. Suppose that single-wavelength phase maps $\varphi_m(x)$ contain phase noise $2\pi\varepsilon_m$ or that surface profiles $z_m(x)$ have a noise level of $\varepsilon_m\lambda_m \sim 12$ nm, where we use $\varepsilon_m = 2\%$ in the simulation. The noise in difference phase map $\varphi_{12}(x)$ is $2\pi\varepsilon_{12} = 2\pi(\varepsilon_1 + \varepsilon_2)$, and that in surface profile $z_{12}'(x)$ is $\varepsilon_{12}\Lambda_{12} \sim 130$ nm. The noise has in effect been amplified by approximately a factor of $2\Lambda_{12}/\lambda_m$, as can be seen from the coarse map, Fig. 4(d), in comparison with Fig. 4(a) or 4(b). The other half of the phase-imaging method consists of an algorithm to reduce the noise back to the level of the single-wavelength phase maps. First, in Fig. 4(e), surface height $z_{12}(x)$ is divided into integer multiples of one of the wavelengths, say, λ_1: $z_{12}''(x) = \text{int}(z_{12}'/\lambda_1)\lambda_1$. Then in Fig. 4(f) we paste on single-wavelength surface map $z_1(x)$: $z_{12}'''(x) = z_{12}'' + z_1$. This almost recovers the surface profile with significantly reduced noise, except at the boundaries of wavelength intervals, where the noise in the single-wavelength phase map causes numerous jumps of size $\pm\lambda_1$. If the noise level is not excessive, one can remove most of the spikes in the last step simply by comparing $z_{12}'''(x)$ with coarse map $z_{12}'(x)$ and, if the difference is more than half of λ_1, adding or subtracting one λ_1, depending on the sign of the difference: $z_{12}(x) = z_{12}''' - \lambda_1 \text{sign}(z_{12}''' - z_{12}')(|z_{12}''' - z_{12}'| > \lambda_1/2)$. Figure 4(g) shows the final result as the fine map, where the noise level is that of $z_1(x)$, or ~12 nm. The remaining spikes in the fine map are due to places where the noise in the coarse map is more than one half of λ_1. That is, the maximum noise level for the method to work properly is given approximately by $\varepsilon_m < \lambda_m/4\Lambda_{12} \sim 4\%$.

Figure 5 shows corresponding curves from a two-wavelength phase-imaging experiment that uses the reflective surface of a resolution target as the object and two wavelengths, at $\lambda_1 = 0.532$ μm and $\lambda_2 = 0.633$ μm. The number of 2π discontinuities in Fig. 5(a) or 5(b) shows that the plane object is tilted by ~3.7 μm in optical path length. We can draw this
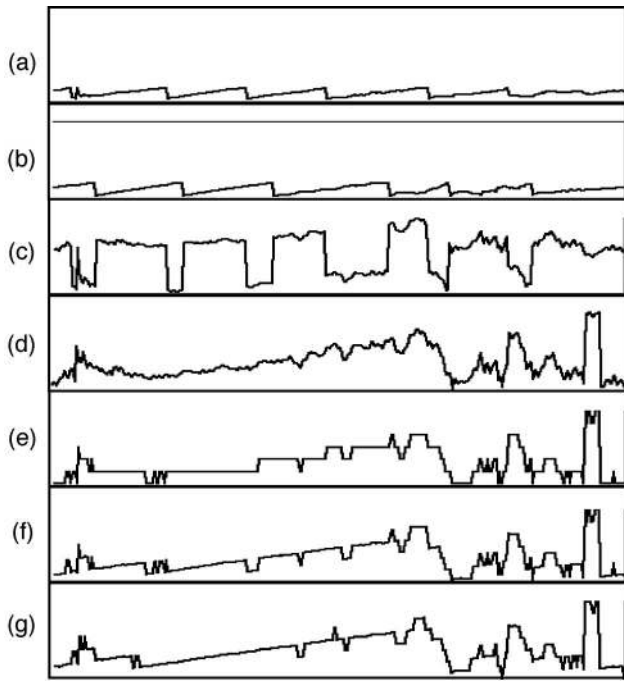
Fig. 5. Experimental profiles of two-wavelength phase-imaging digital holography. The descriptions of the individual figures are the same as for Fig. 6.

$= 0.633$ µm. Figure 6(c) is the coarse map and Fig. 6(d) is the fine map. As they are printed here, the difference between these two is not so obvious, but under close examination of the profiles in a larger format the fine map consists of mostly flat areas peppered with spiky glitches, whereas the coarse map has generally rough surfaces. Apparently the phase noise is not quite small enough to eliminate all the glitches from the fine map.

The method of phase imaging and phase unwrapping works equally well for biological microscopy. In Fig. 7 a 193 µm × 193 µm area of a layer of onion cells is imaged. The single-wavelength phase images of Figs. 7(a) and 7(b) contain numerous 2π discontinuities, making it difficult to discern the cell body and walls. These discontinuities are completely removed in the phase-unwrapped images of Figs. 7(c) and 7(d), and one can clearly observe the cell bodies delineated by the cell walls. The image still contains a fair amount of noise, which can be attributed to a number of possible sources, including quality of optical surfaces in the imaging system, usually characterized as $\lambda/20$; amplitude and phase noise of the reference beam; misregistration of the two images taken with the green and the red lasers owing to slight misalignment of the two beams; and unbalanced dispersion of the two wavelengths in the optical elements of the system. Judging from the high quality of some of the other phase images that we were able to obtain, however, much of what appears to be noise could in fact be the surface features of the slightly withering cells. In any case, it is significant to note that, with such a complex-structured object, conventional phase-unwrapping algorithms would be quite ineffective, whereas the present method is independent of the complexity of the object as long as the noise does not exceed a certain manageable maximum. In Section 5 we consider a technique that can relax the noise limitation even further.

5. Discussion

The phase-unwrapping technique can be further extended to an iterative procedure of three or more wavelengths.[30] First note that axial range Λ_{12} can be increased by use of closer values of λ_1 and λ_2. In Figs. 8(a) and 8(b) we use $\lambda_1 = 0.62$ µm and $\lambda_2 = 0.58$

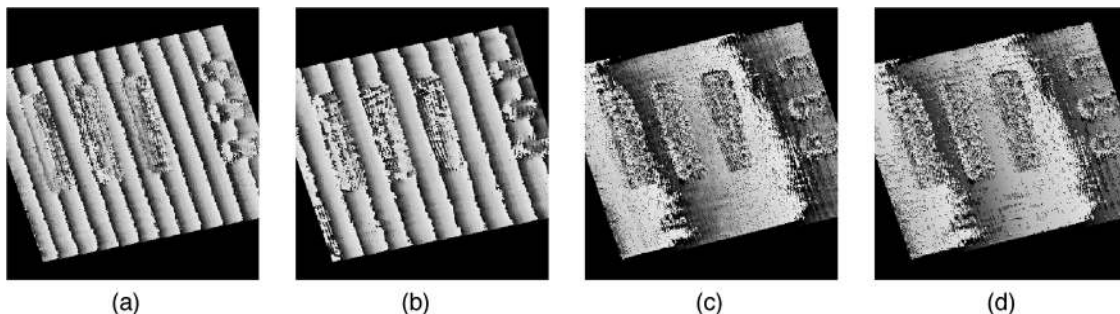conclusion only because we have *a priori* knowledge of the general shape of the object. The phase discontinuity and ambiguity are removed by the combination of the two single-wavelength phase maps, following the procedure outlined above. Recall that the two wavelengths combine to yield the beat wavelength, 3.3 µm, and that the coarse map includes amplified phase noise, both of which are evident from Fig. 5(d). The application of the noise-reducing procedure results in the fine map shown in Fig. 5(g), with significant improvement in the reproduction of the flat areas. Some areas of Fig. 5(a) evidently show more than a few percent phase noise, and these areas do not reproduce well in Fig. 5(d) or 5(g). Figure 6 shows perspective views of phase maps of the surface of a resolution target from another set of experiments. Figures 6(a) and 6(b) single-wavelength phase maps use two wavelengths, $\lambda_1 = 0.532$ µm and λ_2

Fig. 6. Two-dimensional profiles of a resolution target, 157 × 157 µm with 360 × 360 pixels, from two-wavelength phase-imaging digital holography: (a) phase map $z_1(x, y)$ derived from phase $\varphi_1(x, y)$ of $\lambda_1 = 0.532$ µm; (b) phase map $z_2(x, y)$ derived from phase $\varphi_2(x, y)$ of $\lambda_2 = 0.633$ µm; (c) coarse map $z_{12}'(x, y)$; (d) fine map $z_{12}(x, y)$.
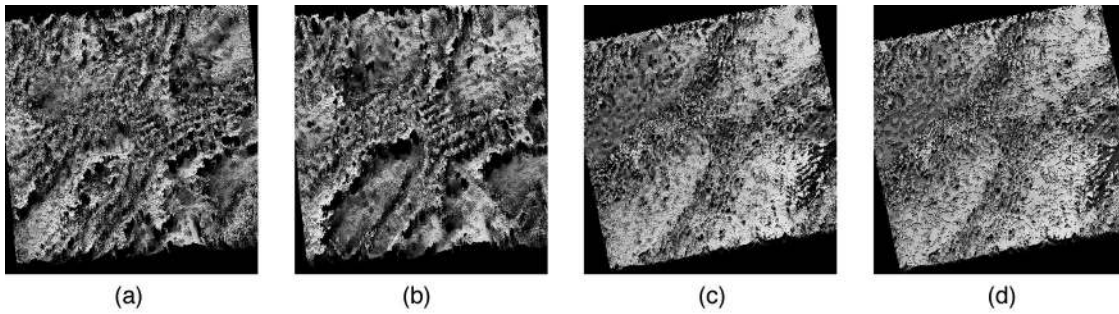
Fig. 7. Two-dimensional profiles of onion cells, 193 μm $\times$ 193 μm with 360 $\times$ 360 pixels, from two-wavelength phase imaging digital holography: (a) phase map $z_1(x, y)$ derived from phase $\varphi_1(x, y)$ of $\lambda_1 = 0.532$ μm; (b) phase map $z_2(x, y)$ derived from phase $\varphi_2(x, y)$ of $\lambda_2 = 0.633$ μm; (c) coarse map $z_{12}'(x, y)$; (d) fine map $z_{12}(x, y)$.

μm, so $\Lambda_{12} = 8.99$ μm. We noted above that for two-wavelength phase imaging the noise limit is given by $\varepsilon_m < \lambda_m/4\Lambda_{12} \sim 1.7\%$: The noise limit is reduced because of the large value of Λ_{12}. In Fig. 8 we use $\varepsilon_m = 5\%$. Figures 8(c) and 8(d) show coarse map z_{12}' and fine map z_{12} generated from λ_1 and λ_2. The noise in the coarse map, $(\varepsilon_1 + \varepsilon_2)\Lambda_{12} \sim 900$ nm, shown in Fig. 8(j), is much larger than half of λ_1, and the fine map has just too many λ_1 high spikes, as shown in Fig. 8(k). Instead, we generate coarse maps z_{13}' and z_{33}' of beat wavelengths Λ_{13} and Λ_{23}, respectively, according to the same procedure as above. With $\lambda_3 = 0.50$ μm we have $\Lambda_{13} = 2.58$ μm and $\Lambda_{23} = 3.63$ μm, Figs. 8(f) and 8(g). Combining these two maps by

using the coarse map procedure produces a coarse map of coarse maps, z_{13-23}', which is actually identical to two-wavelength coarse map z_{12}' of Fig. 8(c). Now, instead of pasting z_1 to z_{12}', which is too noisy to produce a useful result, we go through two steps. First we paste z_{13}' to z_{13-23}' ($=z_{12}'$) to obtain intermediate fine map z_{13-23}'', Fig. 8(h). The noise level in this map is that of z_{13}':$(\varepsilon_1 + \varepsilon_3)\Lambda_{13} \sim 260$ nm, Fig. 8(l). This is now smaller than one half of λ_1, and we can paste z_1 to obtain the final fine map, Fig. 8(i). The noise in this map is that of z_1, $\varepsilon_1\lambda_1 \sim 31$ nm. Thus we achieve long-range, 8.99 μm, phase imaging without discontinuity and with low noise, $\sim$31 nm. The maximum noise level ε_m in the single-wavelength phase
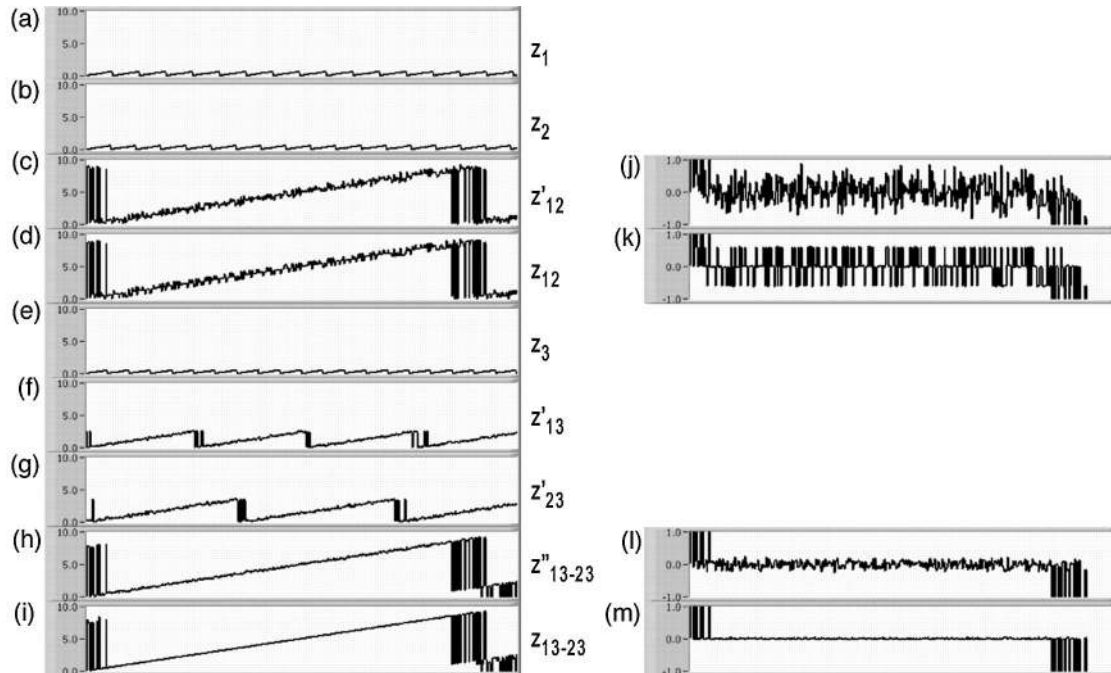

Fig. 8. Simulation of three-wavelength phase-imaging digital holography: (a) height profile $z_1(x)$ of a 10 μm high incline, derived from phase $\varphi_1(x)$ of $\lambda_1 = 0.62$ μm; (b) $z_2(x)$ derived from phase $\varphi_2(x)$ of $\lambda_2 = 0.58$ μm; (c) coarse map $z_{12}'(x)$ of beat wavelength $\Lambda_{12} = 8.99$ μm; (d) fine map $z_{12}(x)$; (e) $z_3(x)$ derived from phase $\varphi_3(x)$ of $\lambda_3 = 0.50$ μm; (f) coarse map $z_{13}'(x)$ of beat wavelength $\Lambda_{13} = 2.58$ μm; (g) coarse map $z_{23}'(x)$ of beat wavelength $\Lambda_{23} = 3.63$ μm; (h) intermediate fine map z_{13-23}'', where $z_{13}'(x)$ is pasted onto $z_{13-23}'(x) = z_{12}'(x)$; (i) final fine map $z_{13-23}(x)$, where $z_1(x)$ is pasted onto $z_{13-23}''(x)$; (j) noise in (c), $z_{12}' - z(x)$, where $z(x)$ is the actual height profile; (k) noise in (d), $z_{12}(x) - z(x)$; (l) noise in (h), $z_{13-23}''(x) - z(x)$; (m) noise in (i), $z_{13-23}(x) - z(x)$. The vertical axis is 10.0 μm full scale in (a)–(i) and 1.0 μm full scale in (j)–(m).
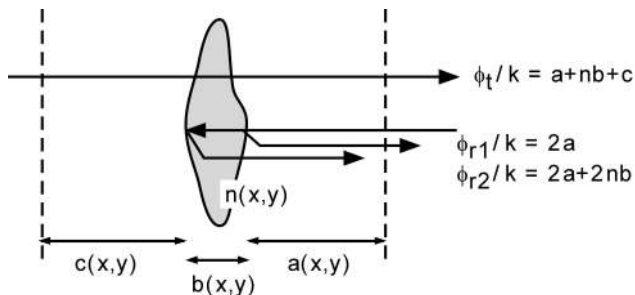
Fig. 9. Object space for reflection and transmission holography.

map for the three-wavelength phase imaging to work is given by the smaller of $\Lambda_{13}/4\Lambda_{12} \sim 7\%$ or $\lambda_1/4\Lambda_{13} \sim 6\%$.

We consider another interesting possibility of acquiring a complete three-dimensional profile of an object by phase-imaging holography. Suppose that a thin transparent object is placed in the object space of the holographic system, Fig. 9. Its physical thickness $b(x, y)$ and index of refraction $n(x, y)$ vary across the transverse direction. Index n does not vary along the axial z direction, or we take n to be the average value along the short z direction. Distances $a(x, y)$ and $c(x, y)$ are measured from arbitrary reference planes on either side of the object. First, a holographic image reconstruction with reflection geometry is carried out. We assume that reflectance r of the object surfaces is small (a few percent) and constant across the surfaces. The reconstructed field is proportional to

$$r \exp(2ika) - r \ \exp[2ik(a + nb)] = \\ -2ir \sin(knb) \exp[ik(2a + nb)]. \qquad (16)$$

From the amplitude variation of the reflected field, one obtains a profile of optical thickness $n(x, y)b(x, y)$. This is substituted into phase map $\varphi_r(x, y) = 2k[a(x, y) - n(x, y)b(x, y)]$ of the reflected field to yield front surface profile $a(x, y)$. Another holography experiment is performed in transmission geometry, which yields another phase map, $\varphi_t(x, y) = k[a(x, y) + n(x, y)b(x, y) + c(x, y)]$. Subtraction of a and nb yields the back surface profile, $c(x, y)$. As the total distance $a + b + c$ is a constant, physical thickness $b(x, y)$ is obtained from $(a + b + c) - a - c$, and this in turn yields index profile $n(x, y)$. If the object thickness is larger than the wavelength, the 2π ambiguity in the phase factors can be resolved by use of the multiwavelength phase-imaging technique presented in this paper. In principle, determination of $n(x, y)b(x, y)$ from $\sin(knb)$ in the amplitude can be handled in a similar fashion, although the amplitude tends to be more sensitive to noise.

6. Conclusions

In this paper we have presented a number of recent experimental results that demonstrate the effectiveness of digital holography in high-resolution biological microscopy. In particular, phase-imaging digital holography offers a highly sensitive and versatile

means to measure and monitor optical path variations. We have presented biological microscopy by two-wavelength phase-imaging digital holography and proposed its extension to three-wavelength phase imaging for longer axial ranges with undiminished resolution. We are in the process of developing a number of digital microholographic techniques to extend its range of applications as in the three-dimensional imaging of cellular structural changes in cell division and tomographic imaging of tissue structures. With continued advances in imaging and computing technology, digital holography is poised to become an important tool for diverse areas of biomedical imaging.

References

1. S. Seebacher, W. Osten, and W. Jueptner, "Measuring shape and deformation of small objects using digital holography," in *Laser Interferometry IX: Applications*, R. J. Pryputniewicz, G. M. Brown, and W. P. O. Jueptner, eds., Proc. SPIE **3479**, 104–115 (1998).
2. W. S. Haddad, D. Cullen, J. C. Solem, J. W. Longworth, A. McPherson, K. Boyer, and C. K. Rhodes, "Fourier-transform holographic microscope," Appl. Opt. **31**, 4973–4978 (1992).
3. E. Cuche, P. Marquet, and C. Depeursinge, "Simultaneous amplitude-contrast and quantitative phase-contrast microscopy by numerical reconstruction of Fresnel off-axis holograms," Appl. Opt. **38**, 6994–7001 (1999).
4. D. Dirksen, H. Droste, B. Kemper, H. Delere, M. Deiwick, H. H. Scheld, and G. von Bally, "Lensless Fourier holography for digital holographic interferometry on biological samples," Opt. Lasers Eng. **36**, 241–249 (2001).
5. W. Xu, M. H. Jericho, I. A. Meinertzhagen, and H. J. Kreuzer, "Digital in-line holography for biological applications," Proc. Natl. Acad. Sci. USA **98**, 11,301–11,305 (2001).
6. I. Yamaguchi, J. Kato, S. Ohta, and J. Mizuno, "Image formation in phase-shifting digital holography and applications to microscopy," Appl. Opt. **40**, 6177–6686 (2001).
7. U. Schnars, "Direct phase determination in hologram interferometry with use of digitally recorded holograms," J. Opt. Soc. Am. A **11**, 2011–2015 (1994).
8. E. Cuche, F. Bevilacqua, and C. Depeursinge, "Digital holography for quantitative phase-contrast imaging," Opt. Lett. **24**, 291–293 (1999).
9. P. Marquet, B. Rappaz, P. J. Magistretti, E. Cuche, Y. Emery, T. Colomb, and C. Depeursinge, "Digital holographic microscopy: a noninvasive contrast imaging technique allowing quantitative visualization of living cells with subwavelength axial accuracy," Opt. Lett. **30**, 468–470 (2005).
10. P. Ferraro, S. De Nicola, A. Finizio, G. Coppola, S. Grilli, C. Magro, and G. Pierattini, "Compensation of the inherent wave front curvature in digital holographic coherent microscopy for quantitative phase-contrast imaging," Appl. Opt. **42**, 1938–1946 (2003).
11. S. Grilli, P. Ferraro, S. De Nicola, A. Finizio, G. Pierattini, and R. Meucci, "Whole optical wave fields reconstruction by digital holography," Opt. Express **9**, 294–302 (2001).
12. U. Schnars and W. P. O. Jueptner, "Digital recording and numerical reconstruction of holograms," Meas. Sci. Technol. **13**, R85–R101 (2002).
13. A. Barty, K. A. Nugent, D. Paganin, and A. Roberts, "Quantitative optical phase microscopy," Opt. Lett. **23**, 817–819 (1998).
14. C. G. Rylander, D. Dave, T. Akkin, T. E. Milner, K. R. Diller,

and A. J. Welch, "Quantitative phase-contrast imaging of cells with phase-sensitive optical coherence microscopy," Opt. Lett. **29,** 1509–1511 (2004).

15. G. Popescu, L. P. Deflores, J. C. Vaughan, K. Badizadegan, H. Iwai, R. R. Dasari, and M. S. Feld, "Fourier phase microscopy for investigation of biological structures and dynamics," Opt. Lett. **29,** 2503–2505 (2004).

16. M. Servin, J. L. Marroquin, D. Malacara, and F. J. Cuevas, "Phase unwrapping with a regularized phase-tracking system," Appl. Opt. **37,** 1917–1923 (1998).

17. M. A. Schofield and Y. Zhu, "Fast phase unwrapping algorithm for interferometric applications," Opt. Lett. **28,** 1194–1196 (2003).

18. Y. Y. Cheng and J. C. Wyant, "Two-wavelength phase shifting interferometry," Appl. Opt. **23,** 4539–4543 (1984).

19. K. Creath, "Step height measurement using two-wavelength phase-shifting interferometry," Appl. Opt. **26,** 2810–2816 (1987).

20. J. Gass, A. Dakoff, and M. K. Kim, "Phase imaging without 2π-ambiguity by multiple-wavelength digital holography," Opt. Lett. **28,** 1141–1143 (2003).

21. I. Yamaguchi, T. Matsumura, and J. Kato, "Phase-shifting color digital holography," Opt. Lett. **27,** 1108–1110 (2002).

22. J. Kato, I. Yamaguchi, and T. Matsumura, "Multicolor digital holography with an achromatic phase shifter," Opt. Lett. **27,** 1403–1405 (2002).

23. N. Demoli, D. Vukicevic, and M. Torzynski, "Dynamic digital holographic interferometry with three wavelengths," Opt. Express **11,** 767–774 (2003).

24. J. W. Goodman, *Introduction to Fourier Optics*, 2nd ed. (McGraw-Hill, 1996).

25. I. Yamaguchi and T. Zhang, "Phase-shifting digital holography," Opt. Lett. **22,** 1268–1270 (1997).

26. T. Zhang and I. Yamaguchi, "Three-dimensional microscopy with phase-shifting digital holography," Opt. Lett. **23,** 1221–1223 (1998).

27. P. Ferraro, S. De Nicola, G. Coppola, A. Finizio, D. Alfieri, and G. Pierattini, "Controlling image size as a function of distance and wavelength in Fresnel-transform reconstruction of digital holograms," Opt. Lett. **29,** 854–856 (2004).

28. F. Zhang, I. Yamaguchi, and L. P. Yaroslavsky, "Algorithm for reconstruction of digital holograms with adjustable magnification," Opt. Lett. **29,** 1668–1670 (2004).

29. M. Jacquot, P. Sandoz, and G. Tribillon, "High resolution digital holography," Opt. Commun. **190,** 87–94 (2001).

30. In principle, it is actually possible to extend the unambiguous axial range beyond beat wavelength Λ_{12} by using two-wavelength phase imaging, though with a stricter requirement on the phase measurement accuracy; see P. de Groot, "Extending the unambiguous range of two-color interferometers," Appl. Opt. **33,** 5948–5953 (1994).